PAPER

Growth mechanism of CH_3NH_3I in a vacuum processed perovskite†

Beom-Soo Kim,[a] Yoonjay Han[a] and Jang-Joo Kim [ID] *[ab]

In the field of halide perovskite research, the growth of high quality films has been a critical issue. Among the reported growth methods, vacuum processes have attracted much attention due to their accurate controllability and high reproducibility, as proven in the manufacture of vacuum deposited organic-light-emitting-diode industry. In a vacuum process, the major difficulty for growing a perovskite film is control of a precursor, methylammonium iodide (MAI), originating from its uncontrollable behavior *i.e.*, a high working pressure and poor adsorption characteristics. Thus, it is crucial to understand the growth mechanism of MAI vapor for the successful application of vacuum processes in the growth of halide perovskite films. In this paper, we report the growth mechanism and deposition kinetics of MAI in a vacuum. Unlike that of conventional materials evaporated in a vacuum, the deposition rate of MAI was found to be much faster on the reactive surface, PbI_2, compared to other non-reactive materials. Surprisingly, a very thin (2 nm-thick) PbI_2 layer increased the initial growth rate of MAI 2.7-fold. Based on the real-time monitored data from a quartz microbalance and surface study, we suggest dipole-induced adsorption as the MAI growth mechanism on PbI_2 and the perovskite in the vacuum process. We believe that this work will provide meaningful insight into film growth in vacuum processed perovskites.

Introduction

MAPbI$_3$-based perovskites (MA = $CH_3NH_3^+$) have attracted considerable attention over the past several years, resulting in solar cells and light-emitting diodes with high efficiency. One of the critical issues in this field is reproducible fabrication of high-quality perovskite films. After Kojima *et al.* (2009) reported a perovskite solar cell produced using a one-step spin-coating process,[1] various methods have been introduced to improve film quality, including sequential deposition,[2,3] solvent engineering,[4,5] vacuum processes,[6–10] hybrid deposition,[11–13] direct contact of methylammonium iodide (MAI) hot powders on lead halides,[14–16] and growth under humid conditions.[17,18] The power conversion efficiency of perovskite solar cells has improved from 3.8% in early studies to over 20% through optimization of the growth conditions, thus demonstrating the importance of perovskite film quality for optoelectronic device applications.[1,4,19–26] A vacuum process is particularly promising and has distinct characteristics from solution processes. For example, high-purity materials can be easily deposited on large-area substrates, eliminating atmospheric effects and solvent exposure for good reproducibility. Additionally, a conformal morphology on

textured Si solar cells can readily be obtained to realize efficient perovskite/silicon tandem solar cells.[27–30] Following Liu's successful application of vacuum processes to perovskite solar cells, several groups have reported perovskite solar cell fabrication using vacuum co-deposition processes;[6–10,31–46] however, controlling and/or calibrating the deposition of MAI is a known to be a difficult problem[7,8,10,31,32,36,40,47–50] and has been attributed to the gas-like behavior of MAI. Several studies have been reported to explain the origin of behaviour of MAI in a vacuum, indicating that the decomposition of MAI, impurities, and variations in adhesion property of MAI can be attributed to the uncontrollable behaviour of MAI in a vacuum process.[51–54] In this regard, accurate monitoring and control over MAI deposition in vacuum processes require a better understanding of the growth mechanism in a vacuum, which is closely related to deposition parameters and perovskite film formation.

In this paper, we report the growth mechanism and resulting deposition kinetics of MAI vapour in a vacuum, which directly affects the deposition parameters and film formation in the vacuum process. MAI showed surface-dependent growth characteristics, which varied for the reactive surface, PbI_2. On the PbI_2 layer, MAI growth is affected by reaction, diffusion, and dipole effects, as evidenced in quartz crystal microbalance (QCM), surface potential microscopy (SPM), and atomic force microscopy (AFM) measurements. Our results suggest that the surface dipoles of the perovskite formed by reacting with the adsorbed MAI trigger the adsorption of polar molecules such as MAI which in turn increases the adsorption rate for film formation in a vacuum.

[a]Department of Materials Science and Engineering, Seoul National University, Seoul, 151-742, South Korea. E-mail: jjkim@snu.ac.kr

[b]Research Institute of Advanced Materials (RIAM), Seoul National University, Seoul, 151-744, South Korea

† Electronic supplementary information (ESI) available. See DOI: 10.1039/d0na00466a

Results and discussion

Table 1 displays the thicknesses of vacuum-deposited MAI on different substrates in the same batch for 60 min at a pressure of 7×10^{-5} Torr. The thicknesses are measured by using a profilometer after scratching the film. Interestingly, the thickness varied remarkably depending on the presence or absence of a PbI$_2$ layer, with relatively small variations on other substrates. The MAI on the PbI$_2$ layer is *ca.* 2.1–2.5 times thicker than on substrates without a PbI$_2$ sub-layer. Here, we speculate that the variation of MAI thickness on different substrates may explain why it is difficult to accurately calibrate MAI thickness or control MAI and/or MAPbI$_3$ deposition in vacuum processes, as reported previously.[7,8,10,31,32,36,40,47–50]

The deposited film thickness also depends on the thickness of the initial PbI$_2$ layers, as shown in Fig. 1. The initial thickness of the PbI$_2$ layer varied from 0, on the indium tin oxide (ITO) surface, to 200 nm; the substrates were exposed to MAI for 60 min at a pressure of 7×10^{-5} Torr (in the same batch). The black line indicates the measured thickness of the film (MAI + PbI$_2$) and the red line represents the thickness change, which is the thickness obtained by subtracting the initial thickness of the PbI$_2$ from the thickness indicated by the black line (MAI + PbI$_2$). Surprisingly, only a 2 nm-thick PbI$_2$ layer resulted in more than twice the MAI film thickness compared to the ITO surface without a PbI$_2$ layer; specifically, the MAI film thickness was 70 nm on ITO and 155 nm on 2 nm-thick PbI$_2$. The MAI thickness showed little change as the PbI$_2$ layer thickness increased from 2 to 200 nm. Deposition of MAI transformed the PbI$_2$ layer into a perovskite film, as shown in Fig. 1b, consistent with the findings of previous reports.[6,7,10,40] X-ray diffraction measurements showed a perovskite (110) peak at 14.2° for 20, 100, and 200 nm-thick PbI$_2$ layers. Notably, the MAI/PbI$_2$ 2 nm-thick film exhibited MAPbI$_3$ perovskite (310) peaks with low intensity at 31.7°. A strong (310) peak is often observed for thin perovskites, such as for perovskite quantum dots,[55] indicating the formation of a thin perovskite layer on the 2 nm-thick PbI$_2$ film; however, the origin of this preferred orientation is not yet clear. The MAI film deposited on ITO showed the same peaks as the films grown on PbI$_2$ layers, but with slightly lower crystallinity. The 200 nm-PbI$_2$ substrate exhibited a strong PbI$_2$ (001) peak at 12.6°, indicating the substantial presence of unreacted PbI$_2$.

To analyze the deposition kinetics, we devised an experiment using two QCMs in a vacuum, as shown in Fig. 2. The two QCM sensors were located side-by-side (only 3 cm apart),
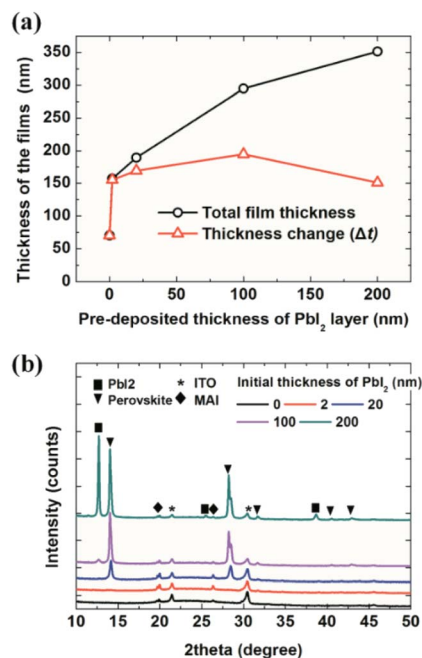

Fig. 1 (a) Thickness of MAI/PbI$_2$ films with respect to the initial PbI$_2$ thickness after a 60 min deposition under a constant MAI working pressure. (b) X-ray diffraction patterns of the MAI layer deposited on PbI$_2$ films of different thicknesses.

approximately 40 cm above the source in the vacuum chamber (Fig. 2a). Only one of the sensors was covered with PbI$_2$ (x nm) *via* vacuum deposition before MAI exposure. Both sensors were then exposed to MAI at a constant working pressure of 7×10^{-5} Torr for 1 h. Fig. 2b shows the monitored weight increase with exposure time on the PbI$_2$ (x nm) QCM. The final deposited weights were 19.6, 34.9, 48.3, 64.4, and 70.5 µg cm^{-2}, as the PbI$_2$ layer thickness increased from 0 to 2, 20, 100, and 200 nm, respectively. It is interesting to note that the weight gain upon exposure to MAI increased with the initial thickness of PbI$_2$, which differed from the thickness change tendencies shown in Fig. 1a. Again, a much larger amount (∼1.8 times) of MAI was deposited on 2 nm-thick PbI$_2$ compared to the bare ITO substrate. Fig. 2c shows the variation in the deposition rate and working pressure with exposure time. The deposition rates increased with the working pressure in the early stages of deposition, reaching a peak value as the working pressure approached the set point of 7×10^{-5} Torr. The rates increased more rapidly to higher peak values with the initial PbI$_2$ layer, and then slowed gradually under the constant working pressure. The deposition rates for the different QCMs reached the same value after ∼40 min. Taken together, understanding the dependence of the deposition rates of MAI on PbI$_2$ layers is a crucial step in resolving the growth mechanism of MAI in a vacuum. We speculate that the deposition characteristics are related to adsorption and diffusion processes of MAI into PbI$_2$ to form MA$_x$PbI$_{2+x}$, or the deposition of MAI if the reaction does not take place, *e.g.*, on ITO or after completion of the conversion from PbI$_2$ to MAPbI$_3$. A much higher deposition rate on the thin 2 nm-thick PbI$_2$ layer compared to the bare ITO substrate

Table 1 Thickness of MAI deposited on different substrates. All of the substrates were exposed to MAI for 60 min at 7×10^{-5} Torr. The thickness of NPB, C60, Au, and PbI$_2$ is 20 nm on an ITO (150 nm)/glass substrate[a]

Substrate	ITO	NPB	C$_{60}$	Au	PbI$_2$
Thickness of MAI (nm)	72	76	85	86	184

[a] MAI: methylammonium iodide (MA = CH$_3$NH$_3^+$); NPB: *N,N'*-di(naphthalene-1-yl)-*N,N'*-diphenyl-benzidine; C60: fullerene; ITO: indium tin oxide.
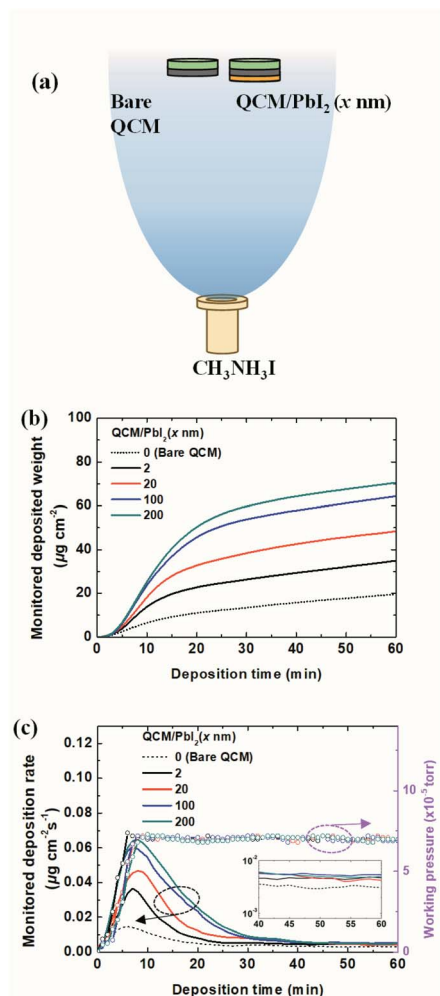
Fig. 2 (a) Schematic figure of a comparative deposition experiment on quartz crystal microbalances (QCMs). (b) The monitored deposited weight of MAI on QCM/PbI$_2$ (x nm). (c) The monitored deposition rate of MAI on QCM/PbI$_2$ (x nm) and working pressures.

suggests an attractive force for MAI adsorption on the PbI$_2$ surface.

A measurement mode that combined AFM with scanning Kelvin probe microscopy (SKPM) was applied to examine the growth characteristics of the films. Thermally evaporated PbI$_2$ on ITO formed smooth films covering the ITO surface, with the exception of the 200 nm-thick PbI$_2$ film, which showed a slightly rougher surface than the thinner layers (Fig. 3a and S2–S4†). Deposition of MAI on the ITO substrate gradually increased the surface roughness, which is relevant to the intrinsic properties of the MAI film deposited on a non-reactive surface. MAI deposition on 2 nm-thick PbI$_2$ resulted in a rapid increase in roughness after 10 min of exposure. In contrast, MAI deposition for 10 min on 20, 100, and 200 nm-thick PbI$_2$ layers did not increase the roughness significantly, and even reduced the roughness of the 200 nm-thick PbI$_2$ layer. This indicates that MAI deposited on PbI$_2$ diffuses into PbI$_2$ to form a perovskite in the early stages. Exposure times longer than 20–30 min increased the roughness, depending on the initial PbI$_2$ thickness, indicating that MAI grows on the perovskite films

after a certain time. Since PbI$_2$ remains after exposure of 100 and 200 nm-thick PbI$_2$ films to MAI (Fig. 1b) for 60 min, the composition of MAI (x value) in MA$_x$PbI$_{(2+x)}$ gradually changed from 0 (PbI$_2$) at the ITO/PbI$_2$ interface to 1 (MAPbI$_3$), followed by deposition of MAI on top of MAPbI$_3$. The transition from perovskite formation to MAI growth on the surface was evidenced by the change in density of the deposited films, as shown in Fig. 3b, which was calculated according to the thickness and weight change of the deposited films (Fig. S5†) for each time interval. The density of MAI, PbI$_2$, and MAPbI$_3$ is 2.22, 4.15, and 6.16 g cm^{-3}, respectively.[36,56,57] Fig. 3b shows that the density of the deposited film decreased gradually, approaching the density of MAI over time. During the first 10 min, the perovskite with x < 1 (or a mixture of perovskite and PbI$_2$) formed for films thicker than 20 nm; the x value decreased with increasing PbI$_2$ thickness. However, MAI was mostly deposited after 30 min, even on the 200 nm-thick PbI$_2$ film, indicating the growth of MAI on MAPbI$_3$. The change in the surface potential of the films as a function of exposure time (Fig. 3c) also provides information on the growth of the perovskite, MAI, or MAI on the perovskite over time. The surface potential is expressed as $V_s = (\phi_{tip} - \phi_{sample})/e$, where V_s is the external voltage applied to the tip to nullify the displacement current, ϕ_{tip} and ϕ_{sample} are the work functions of the tip (Cr/Pt coated tip with a work function of 5.0 eV (ref. 58)) and the sample, respectively, and e is the electronic charge. Measurements of ITO and the PbI$_2$ film before MAI deposition indicated work functions of 4.9 and 5.7 eV, respectively, approximately 0.3 eV higher than the work function obtained by ultraviolet photoelectron spectroscopy (UPS); UPS measures secondary electrons from the Fermi edge with a low-energy cut-off.[59,60] The surface potential of the 2 nm-thick PbI$_2$ film measured by SKPM was 0.1 to 0.2 V higher than that of the thick films. This was attributed to electron transfer from ITO to PbI$_2$, resulting in the Fermi level of PbI$_2$ being closer to the conduction band, thus lowering the work function of PbI$_2$ near the ITO/PbI$_2$ interface. The surface potential of the MAI films on the ITO substrate shifted gradually to 0.4 V, which corresponds to a work function of 4.6 eV for MAI.[60] On thin (2 to 20 nm-thick) PbI$_2$ films, the potential shifted rapidly to 0.2 V during the first 20 min, corresponding to that of MAI, and then followed the same growth trend as that on ITO. The surface potential of MAI-deposited films grown on 100 and 200 nm-thick PbI$_2$ films gradually shifted to ~0.1 V during the first 30 min and then slowly increased to reach 0.3 V at 60 min. Given a reported surface potential of −0.1 V for MAPbI$_3$ using SKPM,[61,62] it can be deduced that the potential change on thick PbI$_2$ involves a change in the surface from PbI$_2$ to the perovskite to MAI, based on roughness and density measurements (Fig. 3a and b).

Interpretation

The growth of MAI on PbI$_2$ in a vacuum can be described in terms of the diffusion of MAI forming MA$_x$PbI$_{2+x}$ with moving boundaries, up to a certain point in time, where this depends on the initial thickness of PbI$_2$, in which x decreases gradually from
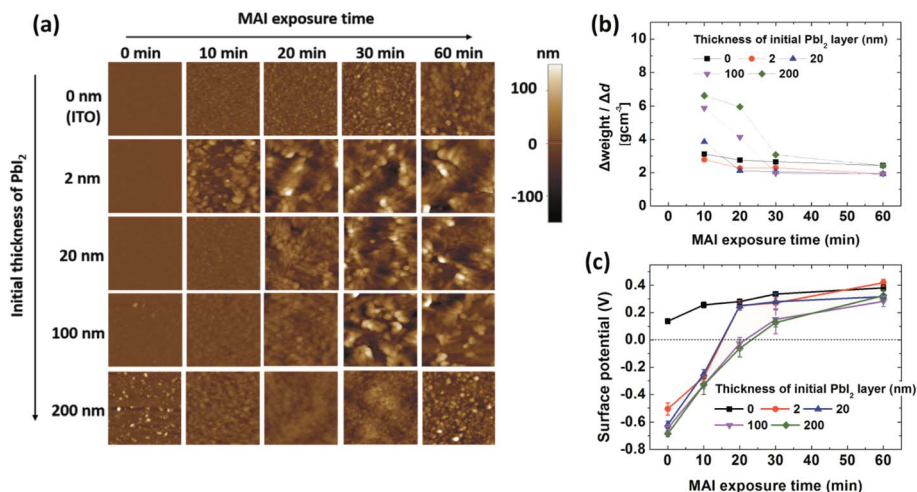
Fig. 3 (a) Topographic images (5 × 5 μm²) and (b) average density of the deposited films calculated according to the weight gain from the QCM and thickness increase from the surface profiler at the given times. (c) Surface potential of the films, as measured by scanning Kelvin probe microscopy (SKPM). Samples of PbI₂ on ITO substrates (PbI₂ thickness: 0, 2, 20, 100, and 200 nm) were exposed to MAI for 0, 10, 20, 30 and 60 min.

the surface toward the film interior, as explained schematically in Fig. 4a. In the early stages of film deposition, the diffusion of MAI into PbI_2 is faster than the deposition of MAI to form MA_xPbI_{2+x} at the surface. However, the diffusion of MAI into PbI_2 slows down over time and MAI eventually begins to grow on MA_xPbI_{2+x} when $x \cong 1$ or slightly higher than 1; in this case, the deposition rate of MAI is higher than the diffusion rate at the perovskite surface. The growth of the perovskite *via* MAI diffusion into thick PbI_2 layers (100 and 200 nm-thick films) results in changes in density and surface potential over time, as shown in Fig. 3b and c, respectively. However, this observation does

not hold for very thin PbI_2 layers, *e.g.*, a 2 nm-thick layer, in which MAI growth is expected within a short time (<10 min). Importantly, therefore, the effects of interdiffusion of MAI into PbI_2 can be excluded to explain this enhanced growth rate, where the surface is fully covered with MAI after converting all of the 2 nm PbI_2. The surface potential shown in Fig. 3c indicates that, however, the MAI potential is negative (−0.3 V) at 10 minutes exposure on the 2 nm PbI_2 substrate. Afterwards, the potential becomes 0.3–0.4 V eventually. This change of surface potential upon the same material, MAI, deposition may originate from the orientation change of polar MAI on the
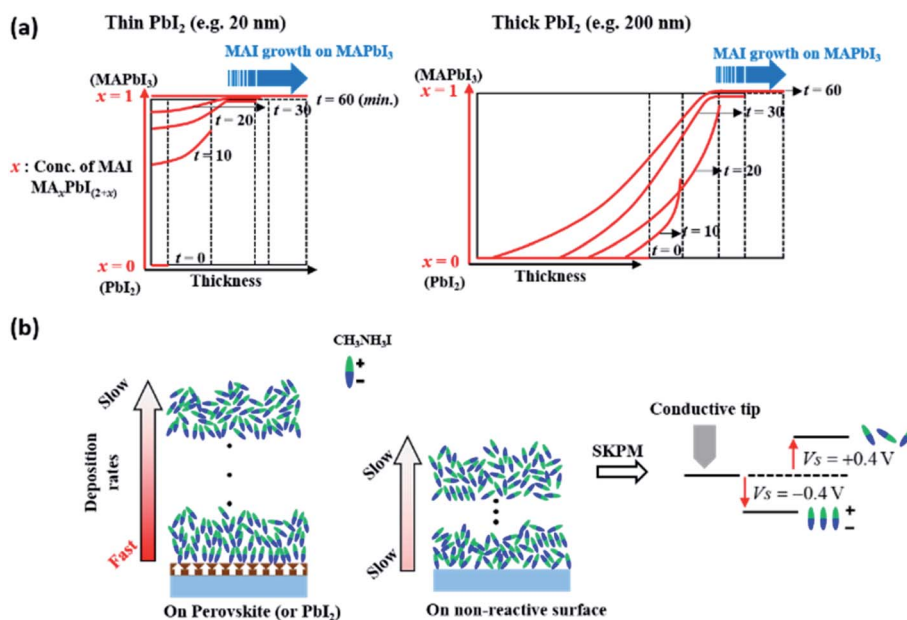

Fig. 4 Schematic illustration of (a) MAI growth with respect to the PbI₂ layer thickness and (b) an interpretation of the change in the surface potential of MAI shown by SKPM.

ferroelectric surface, MAPbI$_3$, as described schematically in Fig. 4b.[63–66] The ordering of MAI decreases gradually with increasing MAI thickness, such that the surface potential of MAI converges to that of bulk MAI. This explains the much higher deposition rate of MAI on very thin 2 nm-thick PbI$_2$ compared to bare ITO (Fig. 1). Specifically, the surface polarization of ferroelectric MAPbI$_3$ attracts MAI molecules *via* a Coulomb interaction or dipole-induced absorption. This observation can be supported by similar reports on enhanced adsorption of gas molecules such as CH$_3$OH, CO$_2$ and CO on an oxide perovskite.[67,68] In these regards, we can conclude that the surface potential changes in Fig. 3c are related to the conversion of PbI$_2$ to MA$_x$PbI$_{2+x}$, combined with the orientation of MAI molecules on the ferroelectric substrate of MA$_x$PbI$_{2+x}$ associated with dipole-induced absorption.

Conclusion

We investigated the growth mechanism of MAI in a vacuum process. MAI showed surface-dependent deposition characteristics that varied significantly in the presence of a reactive surface, PbI$_2$ layer. As the thickness of the PbI$_2$ layer increased, the deposition rate of MAI increased rapidly initially and then decreased to a similar value after a certain time, depending on the initial PbI$_2$ thickness under a constant working pressure. We suggest a dipole-induced adsorption mechanism for MAI in vacuum processes on PbI$_2$ or perovskite. This directly affects the film thickness and the thickness monitor, QCM, which are closely related to deposition parameters of the film fabrication process. Understanding the surface-dependent growth characteristics of MAI is necessary to better control the perovskite film growth in vacuum processes.

Conflicts of interest

There are no conflicts to declare.

Acknowledgements

References

1 A. Kojima, K. Teshima, Y. Shirai and T. Miyasaka, *J. Am. Chem. Soc.*, 2009, **131**, 6050–6051.

2 J. Burschka, N. Pellet, S.-J. Moon, R. Humphry-Baker, P. Gao, M. K. Nazeeruddin and M. Gratzel, *Nature*, 2013, **499**, 316–319.

3 D. Bi, S.-J. Moon, L. Häggman, G. Boschloo, L. Yang, E. M. J. Johansson, M. K. Nazeeruddin, M. Grätzel and A. Hagfeldt, *RSC Adv.*, 2013, **3**, 18762–18766.

4 W. S. Yang, B.-W. Park, E. H. Jung, N. J. Jeon, Y. C. Kim, D. U. Lee, S. S. Shin, J. Seo, E. K. Kim, J. H. Noh and S. I. Seok, *Science*, 2017, **356**, 1376–1379.

5 N. J. Jeon, J. H. Noh, Y. C. Kim, W. S. Yang, S. Ryu and S. I. Seok, *Nat. Mater.*, 2014, **13**, 897–903.

6 M. Liu, M. B. Johnston and H. J. Snaith, *Nature*, 2013, **501**, 395–398.

7 O. Malinkiewicz, A. Yella, Y. H. Lee, G. M. Espallargas, M. Graetzel, M. K. Nazeeruddin and H. J. Bolink, *Nat. Photonics*, 2013, **8**, 128–132.

8 L. E. Polander, P. Pahner, M. Schwarze, M. Saalfrank, C. Koerner and K. Leo, *APL Mater.*, 2014, **2**, 081503.

9 A. S. Subbiah, A. Halder, S. Ghosh, N. Mahuli, G. Hodes and S. K. Sarkar, *J. Phys. Chem. Lett.*, 2014, **5**, 1748–1753.

10 B.-S. Kim, T.-M. Kim, M.-S. Choi, H.-S. Shim and J.-J. Kim, *Org. Electron.*, 2015, **17**, 102–106.

11 L. K. Ono, S. Wang, Y. Kato, S. R. Raga and Y. Qi, *Energy Environ. Sci.*, 2014, **7**, 3989–3993.

12 M. R. Leyden, L. K. Ono, S. R. Raga, Y. Kato, S. Wang and Y. Qi, *J. Mater. Chem. A*, 2014, **2**, 18742–18745.

13 Y. Peng, G. Jing and T. A. Cui, *J. Mater. Chem. A*, 2015, **3**, 12436–12442.

14 Q. Chen, H. Zhou, Z. Hong, S. Luo, H.-S. Duan, H.-H. Wang, Y. Liu, G. Li and Y. Yang, *J. Am. Chem. Soc.*, 2014, **136**, 622–625.

15 J. Zhang, Y. Zhao, D. Yang, C. Li and S. Liu, *RSC Adv.*, 2016, **6**, 93525–93531.

16 X. Zhu, D. Yang, R. Yang, B. Yang, Z. Yang, X. Ren, J. Zhang, J. Niu, J. Feng and S. Liu, *Nanoscale*, 2017, **9**, 12316–12323.

17 J. Yang, B. D. Siempelkamp, D. Liu and T. L. Kelly, *ACS Nano*, 2015, **9**, 1955–1963.

18 G. D. Niu, W. Z. Li, F. Q. Meng, L. D. Wang, H. P. Dong and Y. Qiu, *J. Mater. Chem. A*, 2014, **2**, 705–710.

19 National renewable energy laboratory, Best research-cell efficiency chart, https://www.nrel.gov/pv/cell-efficiency.html.

20 X. Zeng, T. Zhou, C. Leng, Z. Zang, M. Wang, W. Hu, X. Tang, S. Lu, L. Fang and M. Zhou, *J. Mater. Chem. A*, 2017, **5**, 17499–17505.

21 M. Wang, H. Wang, W. Li, X. Hu, K. Sun and Z. Zang, *J. Mater. Chem. A*, 2019, **7**, 26421–26428.

22 T. Zhou, M. Wang, Z. Zang and L. Fang, *Adv. Energy Mater.*, 2019, **9**, 1900664.

23 M. Wang, Z. Zang, B. Yang, X. Hu, K. Sun and L. Sun, *Sol. Energy Mater. Sol. Cells*, 2018, **185**, 117–123.

24 X. Liu, M. Wang, F. Wang, T. Xu, Y. Li, X. Peng, H. Wei, Z. Guan and Z. Zang, *IEEE Electron Device Lett.*, 2020, **41**, 1044–1047.

25 H. Ji, Z. Shi, X. Sun, Y. Li, S. Li, L. Lei, D. Wu, T. Xu, X. Li and G. Du, *ACS Appl. Mater. Interfaces*, 2017, **9**, 42893–42904.

26 Z. Shi, L. Lei, Y. Li, F. Zhang, Z. Ma, X. Li, D. Wu, T. Xu, Y. Tian, B. Zhang, Z. Yao and G. Du, *ACS Appl. Mater. Interfaces*, 2018, **10**, 32289.

27 J. Ávila, C. Momblona, P. P. Boix, M. Sessolo and H. J. Bolink, *Joule*, 2017, **1**, 431–442.

28 P.-S. Shen, Y.-H. Chiang, M.-H. Li, T.-F. Guo and P. Chen, *APL Mater.*, 2016, **4**, 091509.

29 H. Kim, K.-G. Lim and T.-W. Lee, *Energy Environ. Sci.*, 2016, **9**, 12–30.

30 L. K. Ono, M. R. Leyden, S. Wang and Y. Qi, *J. Mater. Chem. A*, 2016, **4**, 6693–6713.

31 Q. Lin, A. Armin, R. C. R. Nagiri, P. L. Burn and P. Meredith, *Nat. Photonics*, 2014, **9**, 106–112.

32 T.-W. Ng, C.-Y. Chan, M.-F. Lo, Z. Q. Guan and C.-S. Lee, *J. Mater. Chem. A*, 2015, **3**, 9081–9085.

33 C. Gao, J. Liu, C. Liao, Q. Ye, Y. Zhang, X. He, X. Guo, J. Mei and W. Lau, *RSC Adv.*, 2015, **5**, 26175.

34 D. T. C. Tran, Y. Liu, E. S. Thibau, A. Llanos and Z.-H. Lu, *AIP Adv.*, 2015, **5**, 087185.

35 J. Borchert, H. Boht, W. Fränzel, R. Csuk, R. Scheer and P. Pistor, *J. Mater. Chem. A*, 2015, **3**, 19842.

36 J. Teuscher, A. Ulianov, O. Müntener, M. Grätzel and N. Tetreault, *ChemSusChem*, 2015, **8**, 3847–3852.

37 Z. Su, F. Hou, F. Jin, L. Wang, Y. Li, J. Zhu, B. Chu and W. Li, *Org. Electron.*, 2015, **26**, 104–108.

38 W. Ke, D. Zhao, C. R. Grice, A. J. Cimaroli, G. Fang and Y. Yan, *J. Mater. Chem. A*, 2015, **3**, 23888–23894.

39 C. Momblona, L. Gil-Escrig, E. Bandiello, E. M. Hutter, M. Sessolo, K. Lederer, J. Blochwitz-Nimoth and H. J. Bolink, *Energy Environ. Sci.*, 2016, **9**, 3456–3463.

40 B.-S. Kim, M.-H. Choi, M.-S. Choi and J.-J. Kim, *J. Mater. Chem. A*, 2016, **4**, 5663–5668.

41 D. Zhao, W. Ke, C. R. Grice, A. J. Cimaroli, X. Tan, M. Yang, R. W. Collins, H. Zhang, K. Zhu and Y. Yan, *Nano Energy*, 2016, **19**, 88–97.

42 L. Calió, C. Momblona, L. Gil-Escrig, S. Kazim, M. Sessolo, Á. Sastre-Santos, H. J. Bolink and A. Shahzada, *Sol. Energy Mater. Sol. Cells*, 2017, **163**, 237–241.

43 H.-J. Song, H. Lee, S. Ahn, H. Song and C. Lee, *Jpn. J. Appl. Phys.*, 2018, **57**, 102303.

44 V. Arivazhagan, J. Xie, Z. Yang, P. Hang, M. M. Parvathi, K. Xiao, C. Cui, D. Yang and X. Yu, *Sol. Energy*, 2019, **181**, 339–344.

45 H. Xu, F. Xu, W. Wang, Y. Zhu, Z. Fang, B. Yao, F. Hong, J. Cui, F. Xu, R. Xu, C.-C. Chen and L. Wang, *Org. Electron.*, 2019, **69**, 329–335.

46 R. Kottokkaran, H. A. Gaonkar, H. A. Abbas, M. Noack and V. Dalal, *J. Mater. Sci.: Mater. Electron.*, 2019, **30**, 5487–5494.

47 C. W. Chen, H. W. Kang, S. Y. Hsiao, P. F. Yang, K. M. Chiang and H.-W. Lin, *Adv. Mater.*, 2014, **26**, 6647–6652.

48 D. Yang, Z. Yang, W. Qin, Y. Zhang, S. Liu and C. Li, *J. Mater. Chem. A*, 2015, **3**, 9401–9405.

49 S.-Y. Hsiao, H.-L. Lin, W.-H. Lee, W.-L. Tsai, K.-M. Chiang, W.-Y. Liao, C.-Z. Ren-Wu, C.-Y. Chen and H.-W. Lin, *Adv. Mater.*, 2016, **28**, 7013–7019.

50 S. Wang, L. K. Ono, M. R. Leyden, Y. Kato, S. R. Raga, M. V. Lee and Y. Qi, *J. Mater. Chem. A*, 2015, **3**, 14631–14641.

51 L. Liu, J. A. McLeod, R. Wang, P. Shen and S. Duhm, *Appl. Phys. Lett.*, 2015, **107**, 061904.

52 S. Olthof and K. Meerholz, *Sci. Rep.*, 2017, **7**, 40267.

53 J. Borchert, I. Levchuk, L. C. Snoek, M. U. Rothmann, R. Haver, H. J. Snaith, C. J. Brabec, L. M. Herz and M. B. Johnston, *ACS Appl. Mater. Interfaces*, 2019, **11**, 28851.

54 K. B. Lohmann, J. B. Patel, M. U. Rothmann, C. Q. Xia, R. D. J. Oliver, L. M. Herz, H. J. Snaith and M. B. Johnston, *ACS Energy Lett.*, 2020, **5**, 710–717.

55 J. H. Im, C. R. Lee, J. W. Lee, S. W. Park and N. G. Park, *Nanoscale*, 2011, **3**, 4088–4093.

56 O. Yamamuro, M. Oguni, T. Matsuo and H. J. Suga, *Chem. Thermodyn.*, 1986, **18**, 939.

57 J. Huang, K. Jiang, X. Cui, Q. Zhang, M. Gao, M. Su, L. Yang and Y. Song, *Sci. Rep.*, 2015, **5**, 15889.

58 R. Vidyasagar, B. Camargo, E. Pelegova, K. Romanyuk and A. L. Kholkin, *Ferroelectrics*, 2017, **508**, 115.

59 J. S. Kim, B. Lagel, E. Moons, N. Johansson, I. D. Baikie, W. R. Salaneck, R. H. Friend and F. Cacialli, *Synth. Met.*, 2000, **111**, 311.

60 T.-W. Ng, H. Thachoth Chandran, C.-Y. Chan, M.-F. Lo and C.-S. Lee, *ACS Appl. Mater. Interfaces*, 2015, **7**, 20280–20284.

61 J. R. Harwell, T. K. Baikie, I. D. Baikie, J. L. Payne, C. Ni, J. T. S. Irvine, G. A. Turnbull and I. D. W. Samuel, *Phys. Chem. Chem. Phys.*, 2016, **18**, 19738–19745.

62 K. Song, Y. Wu, X. Chen, Y. He, L. Liu, G. Chen and R. Liu, *AIP Adv.*, 2018, **8**, 035114.

63 Y. Li, M. Behtash, J. Wong and K. Yang, *J. Phys. Chem. C*, 2018, **122**, 177–184.

64 J. Lahnsteiner, G. Kresse, A. Kumar, D. D. Sarma, C. Franchini and M. Bokdam, *Phys. Rev. B*, 2016, **94**, 214114.

65 Y. Rakita, O. Bar-Elli, E. Meirzadeh, H. Kaslasi, Y. Peleg, G. Hodes, I. Lubomirsky, D. Oron, D. Ehre and D. Cahen, *Proc. Natl. Acad. Sci. U. S. A.*, 2017, **114**, E5504.

66 S. Duhm, G. Heimel, I. Salzmann, H. Glowatzki, R. L. Johnson, A. Vollmer, J. P. Rabe and N. Koch, *Nat. Mater.*, 2008, **7**, 326.

67 D. Li, M. H. Zhao, J. Garra, A. M. Kolpak, A. M. Rappe, D. A. Bonnell and J. M. Vohs, *Nat. Mater.*, 2008, **7**, 473–477.

68 L. C. Tănase, N. G. Apostol, L. E. Abramiuc, C. A. Tache, L. Hrib, L. Trupină, L. Pintilie and C. M. Teodorescu, *Sci. Rep.*, 2016, **6**, 35301.